Sepiolite/Fe_3O_4 composite for effective degradation of diuron

Kai Hou[a,b,c], Gaofeng Wang[b,c], Yanping Zhu[b,c], Naeim Ezzatahmadi[b,c], Liangjie Fu[a,d*], Aidong Tang[e], Huaming Yang[a,d*], Yunfei Xi[b,c*]

[a] *Centre for Mineral Materials, School of Minerals Processing and Bioengineering, Central South University, Changsha 410083, China*

[b] *School of Earth, Environmental and Biological Sciences, Science and Engineering Faculty, Queensland University of Technology (QUT), Brisbane, QLD 4001, Australia*

[c] *Institute for Future Environments, Science and Engineering Faculty, Queensland University of Technology (QUT), Brisbane, QLD 4001, Australia*

[d] *Hunan Key Lab for Mineral Materials and Application, Central South University, Changsha 410083, China*

[e] *School of Chemistry and Chemical Engineering, Central South University, Changsha 410083, China*

[*] *Corresponding authors, Email: hmyang@csu.edu.cn (H.Y.), franch@csu.edu.cn (L.F.), y.xi@qut.edu.au (Y.X.), Fax: 86-731-88710804, Tel.: 86-731-88830549*

Abstract: A novel sepiolite-supported Fe_3O_4 magnetite (SepMag) composite was prepared for diuron degradation. The samples were characterized by X-ray powder diffraction (XRD), X-ray fluorescence (XRF), Fourier transform infrared spectroscopy (FTIR), N_2 adsorption-desorption and BET surface area analysis, scanning electron microscope (SEM) as well as transmission electron microscope (TEM). The chemical state of Fe in SepMag composite before and after degradation experiments was characterized by X-ray photoelectron spectroscopy (XPS). The enhanced degradation efficiency for diuron was attributed to the effective generation of hydroxyl radical in ultrasound/SepMag/H_2O_2 system. The degradation rate of diuron depended upon the composite amount, hydrogen peroxide dosage, initial pH of solution and temperature. The degradation reaction was also optimized by changing the ultrasound intensity and Fe_3O_4 content in the composites. Moreover, mineralization and degradation pathway were evaluated on the basis of total organic carbon and liquid chromatography mass spectrometry. It was confirmed that with the assistance of ultrasound treatment SepMag composite has potential advantages for the removal of diuron from aqueous solution.

Keywords: sepiolite; Fe_3O_4; composite; diuron; degradation

1. Introduction

Pesticides and herbicides are widely used to eliminate and control pests and weeds. As a double-edged sword, only less than 10% of the sprayed pesticides have reached their targets, while other pesticides persist in the soil and reach the water bodies via agricultural run-off, causing species extinction and symptoms of pesticide poisoning every year (Rawtani et al., 2018). Take the Great Barrier Reef (GBR) as an example; GBR, is the largest and one of the most iconic coral reef ecosystems on earth located in Australia. Despite the fact that protection of coral reef started from 1975, coral cover in the GBR has declined by over 50% in the past 30 years. Among the various stressors that affect the GBR, the residual pesticides adversely impact water quality in GBR and neighboring ecosystem. As photosynthesis inhibitors, herbicides have toxic effects on seagrasses as well as the symbiotic microalgae of coral reefs (De Valck and Rolfe, 2018). Herbicides and insecticides applied to agricultural crops may also pose a threat to non-target species, causing behavior alterations, cytotoxic and genotoxic responses, DNA mutations and endocrine disruption, which may in turn threaten human health through food chain (Allan et al., 2017; Rowen et al., 2017). Therefore, in "Reef 2050 Long-Term Sustainability Plan" launched by the Australian and Queensland Governments, the aim of at least a 60% reduction in end-of-catchment pesticide loads in priority areas was set up. Diuron is one kind of herbicides that inhibits photosystem II (PSII inhibitors). Diuron (N'-[3,4-dichlorophenyl]-N,N-dimethylurea) belongs to the phenyl amide family and the subclass of phenyl urea, which was widely used in Queensland to control a wide variety of annual and perennial broadleaf and grassy weeds (Juana Ma Rosas, 2014). It is relatively persistent in soil with half-lives up to 1 year, and is found in adjacent waterways and marine waters of the GBR as well as other parts of the world. By measurement, diuron contents in more than 5 waterways that discharge to the GBR are regularly exceeded (Allan et

al., 2017; Warne et al., 2018).

There are many conventional techniques, such as adsorption, flocculation, and coagulation (Zhang et al., 2018), for the elimination of herbicides from aqueous medium. These methods are effective for the removal of herbicides but fail in their complete mineralization. Advanced oxidation processes (AOPs) have several advantages over the conventional techniques such as fast reaction, moderate reaction condition and easy operation. Various AOPs including electrochemical (Khongthon et al., 2016), photo catalytic (Oturan et al., 2011), photocatalytic ozonation (Solís et al., 2016), and Fenton-like process (Vicente et al., 2012; Zhou et al., 2013; Rosas et al., 2014), were reported for the degradation of diuron. However, few studies were reported to combine the Fenton reaction and ultrasound irradiation for the degradation of diuron. Ultrasonic irradiation is unique AOPs as it generates hydroxyl radicals directly from water molecules which immensely contributed to the Fenton reaction process for diuron degradation (Mahamuni and Adewuyi, 2010).

Although there are many phases of iron oxide in nature, the most popular ones in water research are the nanoscale zero-valent iron (nZVI), Fe_3O_4 (Mag) and γ-Fe_2O_3. Mag, a ferromagnetic iron oxide, has been the most extensively studied. Mag particles, used as adsorbents and catalysts for target species, can be easily isolated from sample solutions using an external magnetic field (Fayazi et al., 2015). There are three fabrication techniques of magnetic nanoparticles including physical, wet chemical preparation and microbial methods (Hajba and Guttman, 2016). Amongst them, the wet chemical preparation especially co-precipitation method is most common used. The major advantage of the co-precipitation method is that the nanocomposites can be rapidly prepared by a simple pathway. However, the control of the size distribution and dispersibility of Mag nanoparticles are still challenging issues (Chen et al., 2016). Clay minerals were widely used as support materials for functional particles and drug (Li et al., 2016; Zhang et al., 2016; Peng et al., 2017; Yan et al., 2018; Zhao

et al., 2019), also for Mag nanoparticles (Mohammed et al., 2017), and the prepared Mag/clay composites have been applied to many fields, such as environmental application (Yuan et al., 2010; Chang et al., 2016; Middea et al., 2017; Yuan, 2017), engineering (Marins et al., 2015; Chen et al., 2017; Liu et al., 2017) and medicine (Mao et al., 2016; Long et al., 2018; Nasrabadi et al., 2018). Sepiolite is a fibrous 2:1 type clay mineral, formed by an alternation of blocks and tunnels that grow up in the fiber direction with a particle size in the 0.2–2 μm length, 100-300 nm in width and 50-100 nm thickness range (Gonzalez-Alfaro et al., 2011). It has captured much attention because of its low-cost, high chemical stability, large specific surface area and large thermal stability (Ma et al., 2017; Hou et al., 2017; Jeon et al., 2018). So far, Mag anchored Sep nanofibers have been successfully synthesized as adsorbents (Yu et al., 2016; Ahribesh et al., 2017; Puente-Urbina and Montero-Campos, 2017), photocatalyst (Akkari et al., 2017), and magnetorheological material (Dong et al., 2017).

In this paper, novel SepMag composites were synthesized, and the prepared samples were characterized by multiple methods. Fenton reaction accompanied with ultrasound irradiation technique was employed to degrade diuron, and degradation pathway were also studied with this coupling technology. The objective of the present work is to synthesize and characterize the SepMag composites and to investigate the effects of initial pH, sample and H_2O_2 amounts, temperature, Mag content in SepMag and ultrasound intensity on degradation efficiency. The reactive species and possible oxidation pathways of diuron in the system was also discussed.

2. Experimental

2.1 Materials

The pristine sepiolite (denoted as Sep) in powder form was purchased from Hebei province (China). Diuron, hydrogen peroxide (H_2O_2, 34.5-36.5 %), ferric chloride ($FeCl_3 \cdot 6H_2O$) and

ferrous chloride ($FeCl_2 \cdot 4H_2O$) were purchased from Sigma Aldrich. The acid treated sepiolite (SepH) was prepared as follows: Sep was dispersed into 1M HCl to form a suspension (20 g/L), followed by stirring for 24 h. Then, the suspension was centrifuged and rinsed several times by deionized water. The obtained powder was dried at 80 °C for 12 h, grounded by a Retsch mill and stored in a desiccator before use.

2.2 Sample synthesis

Deionised water was used in all experiments and was purged using N_2 for at least 30 min prior to use. Magnetite (Mag) particles were synthesized by the slow co-precipitation method reported previously (Lenders et al., 2015; Nor et al., 2016; Arshad et al., 2018). Sepiolite-supported Fe_3O_4 magnetite (SepMag) composites were prepared as follows: Appropriate amounts of $FeCl_3$, $FeCl_2 \cdot 4H_2O$ (1:1 in mole ratio) and acid pretreated Sep (SepH) powder were suspended in 500 mL of deoxygenated deionized water to obtain the precursor solution. Then the precursor solution was heated at 85 °C with continuously mechanical agitation in nitrogen atmosphere for 1 h. Next, 100 mL 12.5 % NH_3 solution was added to the precursor solution drop by drop, under constant stirring for 1 h. The prepared black powder was collected by centrifugation at 2000 rpm and then washed with 200 mL deoxygenated deionized water and dried using a freeze dryer. Finally, the obtained sample was kept in a vacuum desiccator prior to use. The synthesis process is illustrated in **Fig. 1**. The designed Mag loading content of SepMag composites were 40%, 60% and 80%, respectively, and the actual value of Mag in each SepMag composite was measured by XRF) to be 43%, 61% and 78%, respectively. The SepMag composites with different Mag loadings were marked as x-SepMag, where x stands for Mag percentage content.

2.3 Characterization

Powder X-ray diffraction (XRD) patterns were collected using a PANalytical X'Pert Pro diffractometer operating in Bragg-Brentano geometry with a cobalt source (40 kV, 40 mA, λ =

1.79021 Å). Patterns were collected from 4 to 90° at a step size of 0.016°. The chemical compositions of tested samples were determined by an EDXRF analyzer (ARL Quant'x, Thermo Scientific) in QUT. Fourier transform infrared (FTIR) spectroscopy was obtained using a Nicolet Nexus 870 FTIR spectrometer equipped with a diamond ATR accessory. Spectra over ranged from 4000 to 400 cm^{-1} were obtained by the co-addition of 64 scans with a resolution of 4 cm^{-1} and a mirror velocity of 0.6329 cm/s. X-ray photoelectron spectroscopy (XPS) analyses were carried out on a Thermo Scientific K-Alpha spectrometer equipped with Al Ka source (1486.8 eV), the spectra were collected with pass energy of 30 eV and an analysis area of 400 μm^2. The C1s peak at 284.8 eV was used as a reference to correct the charging effect. All spectra were performed with smart background correction. Nitrogen adsorption–desorption isotherm was measured at -196 °C on a Micromeritics Tristar II 3020 system. Brunauer−Emmett−Teller (BET) method was utilized to calculate the specific surface areas. The total pore volume was calculated from the amount adsorbed at a maximum relative pressure (P/P_0). Prior to measurements, the samples were degassed at 110 °C under vacuum for 24 hours. Scanning electron microscope (SEM) images were taken using Tescan MIRA3 SEM operated at 10 kV (the samples were coated with gold prior the experiment) and transmission electron microscopy (TEM) images were taken with a JEOL-1400 instrument in QUT.

2.4 Degradation experiments

Diuron remediation experiments were carried out at room temperature with specific pH value adjusted from 2 to 9 with HCl and NaOH. In a typical experiment, a sample (0.5 g/L) was weighed and added to a beaker containing 30 mL of 30 mg/L diuron solution. After 20 min dark reaction, a given volume of 30% H_2O_2 was added to the above suspension to initiate the reaction. The suspension was then stirred or ultrasound (600W, 40kHz) treated for a pre-set time. Circulating water and heating apparatus were used for sonicator to control the

159 temperature, in order to investigate the effects of temperature on diuron removal rate, the
160 temperatures were set from 20 °C to 60 °C, in other experiments the temperatures were set as
161 20 °C. Upon completion of the reaction, 1 mL of supernatant was withdrawn using a pipette,
162 and injected into a 2 mL amber glass vial containing 10 µL of 2 M Na_2SO_3 solution, to quench
163 any hydroxyl radical reaction (Ma et al., 2016b). The concentration of the target diuron was
164 freshly quantitatively analyzed using an Agilent HP1100 HPLC equipped with a Waters, 5µ,
165 C18 column (4.6 mm × 250 mm) and a UV absorbance detector operating at 254 nm. A
166 mobile phase of methanol–water (70:30) at a flow rate of 0.7 mL/min and 20 µL of injection
167 volume was used for this experiment (Oturan et al., 2011). The removal efficiency of diuron
168 was calculated by Equation 1:

169 $$\eta = \frac{C_i - C_t}{C_i} \times 100\% \quad (1)$$

170 Where η (%) is diuron removal efficiency, C_i is initial diuron concentration (mg/L), and C_t is
171 diuron concentration at t min (mg/L). LC-MS data were acquired using a Dionex3000
172 Ultimate HPLC coupled to an ion trap mass spectrometer (LTQ-XL, Thermo Fisher Scientific,
173 Bremen, Germany) with an electrospray ionisation source operating in the positive ion mode.
174 TOC concentration was measured by a Shimadzu TOC-V analyser using zero grade air as a
175 carrier gas.
176

177 ## 3. Results and discussion

178 To study possible changes in crystal phase and grain size, the XRD patterns of Sep, SepH and
179 SepMag were measured (**Fig. 2**). Based on the reflections, for SepH, the calcite and dolomite
180 impurities disappeared after acid pretreatment, while some talc remained. The intact main
181 reflections of Sep indicated negligible influence of acid pretreatment on the crystal structure
182 of Sep. For SepMag, the broad reflections of Mag indicated the small particle size of Mag in
183 SepMag composites (Zhou et al., 2016; Dong et al., 2018). As seen from the XRD patterns,

184 the five main peaks of sepiolite (Sep) at 8.49°, 22.89°, 23.91°, 27.67° and 33.35° shifted
185 slightly to 8.62°, 23.01°, 24.06°, 27.74° and 33.49° after acid treatment (SepH), respectively.
186 The small variations in 2 theta values of the peaks can be caused by the lattice expansion due
187 to the lixiviation of Mg from the sepiolite structure and this is further confirmed by XRF (See
188 **Table S2-S3**).

189 FTIR spectroscopy is performed to study the surface groups in bare Mag and Sep loaded
190 Mag particles (**Fig. 3**). The adsorption bands between 3700~3000 and 1640 cm^{-1} indicated
191 the stretching vibrations and bending vibration of O-H bond (Shahid et al., 2018). The bands
192 at 1020 and 460 cm^{-1} were attributed to symmetrical stretching vibration of Si-O-Si and the
193 band at 1210, 1080 and 980 cm^{-1} represented bending vibration of Si-O bond. For the
194 SepMag composite, the broadening and overlapping of these small bands indicated the
195 variation of these Si-O bonds. The strong characteristic bands of Fe-O groups appeared at
196 around 550 cm^{-1} indicated the formation of Mag particles (Singh et al., 2018). The weakened
197 bands of Fe-O in SepMag composite could be related to the dilution effects as well as the
198 interface bonding between sepiolite surface and Mag particles. The stretching band of silanol
199 (Si-OH) group at 3720 cm^{-1}, dealing with the bonding of nanoparticles to sepiolite (Akkari et
200 al., 2016), was not observed possibly due to the absence of KBr and pressing for the samples.
201 Instead, the stretching band of external surface Si-OH at 3675 cm^{-1} was found in SepH, but it
202 disappeared in SepMag. It can be assumed that these groups are in hydrogen bonding
203 interaction with magnetite (Akyuz et al., 2010).

204 The BET isotherms of Sep, SepMag and Mag and their respective textural value have
205 been presented in **Fig. 4**. The BET isotherm of the materials possessed a type IV isotherm
206 with well-defined hysteresis loop which indicated that the materials were mesoporous in
207 nature. SepMag composite (104.79 m^2/g) had lower surface area than SepH (152.15 m^2/g), but
208 higher than Mag (96.96 m^2/g). Furthermore, the microporous surface area of SepH (~66 m^2/g)

209 is much lowered after Mag loading. The calculated microporous surface area of SepMag is ~7
210 m^2/g, which is because the Mag nanoparticles covering the surface of SepH may block the
211 entry to the tunnels (Akkari et al., 2016).

212 And the SepMag composite (5.99 nm) had lower average pore width than Mag (6.36 nm)
213 but higher than SepH (5.38 nm). The surface area decreased slightly due to the covering of
214 Mag particles on clay surface (Vengatesan et al., 2017). The large pore width of Mag and
215 SepMag indicated the structural construction of clay stacking with plenty of Mag particles.

216 The SEM image of Sep shows the flat and straight fibres of Sep (**Fig. 5**a). The lump-like
217 morphology of synthetic Mag particles indicates large size of these particles usually from 5 to
218 50 μm diameter (**Fig. 5**b). After dispersing the Mag particles onto Sep surface, the grain
219 diameter of Mag was distinctly decreased. The Mag particles with lesser diameter are well
220 dispersed and stabilized on the surface of Sep (**Fig. 5**c). The size of Mag particles on Sep
221 surface is 5-20 nm by TEM analysis (**Fig. S1**). Sep fibers have a positive impact on Mag
222 dispersion and average diameter reduction. The elemental distribution mapping of SepMag
223 was investigated with TEM analysis (**Fig. 6**). The homogenous distribution of Sep with good
224 dispersibility agrees well with the SEM images. In addition to O, Si and Mg elements of the
225 acid pre-treated Sep, the Fe element is uniformly distributed on the surface of Sep, and the O
226 element comes from both the SepH structure and the Mag particles, which shows the insertion
227 of Mag particles onto the surface of Sep without affecting their morphology.

228 The amount of diuron adsorbed on centrifuge tube, syringe and syringe filter was found
229 to be negligible. The adsorption amount of diuron onto the SepMag is around 20 % after 20
230 min stirring (**Fig. 7**), due to the large specific surface area of Sep. The effect of initial pH on
231 the degradation of diuron was examined. After adding 20 mM of H_2O_2, the catalytic reaction
232 started and the optimum pH is around 3. At low pH, the reduction in efficiency is likely
233 caused by ferrous ions $[Fe(H_2O)_6]^{2+}$ species which slowly produces •OH (Kuo, 1992). When

pH is above 3, the degradation efficiency decreased significantly. This is possibly ascribed to the formation of relatively inactive ferryl ion (FeO^{2+}) as described in Reaction 2 (Yang et al., 2015).

$$Fe^{2+} + H_2O_2 \rightarrow FeO^{2+} + H_2O \quad (2)$$

These results show that the degradation of diuron is strongly dependent on the pH of the solution. The diuron removal efficiency increases with use of more composite amount from 0.1 g/L to 5 g/L (**Fig. 7**b). There is an evidently increase in removal efficiency from 36.7 to 86.9 % when the amount of SepMag increases from 0.1 to 1 g/L, indicating that the sample concentration lower than 1 g/L is not sufficient for the removal of diuron. The removal rate increased slowly between 1 g/L and 5 g/L indicating the optimum amount for SepMag was 1 g/L if considering the economic factor.

The effect of hydrogen peroxide dosage on diuron removal percentage is measured at partly optimized condition (pH 3, 25 °C, 300 W ultrasound power and 1 g/L 61-SepMag). With the increasing dosage of H_2O_2, the removal of diuron increases quickly until the H_2O_2 dosage reaching 40 mM (**Fig. 7**c). The deficiency of •OH generated by H_2O_2 causes the low degradation of organic pollution. On the contrary, excessive H_2O_2 concentration is not encouraged when considering investment costs (Wang et al., 2016; Burgos-Castillo et al., 2018). Hydrogen peroxide can also influence the pH of solution (Ma et al., 2016b). So 40 mM is the appropriate hydrogen peroxide dosage. Diuron degradation were tested at five different temperatures from 20 °C to 60 °C (pH 3, 40 mM H_2O_2 dosage, 1 g/L 61-SepMag dosage and 300 W ultrasound power), the results show that the degradation of diuron is strongly dependent (almost linearly) on the temperature of the solution (**Fig. 7**d). Though heating the water is power-wasting in practical use, these measurements are key to estimate the best time and season (noon and afternoon in summer) for industrial application regardless of evaporation of diuron (Ma et al., 2016a).

The effect of Mag content on the diuron degradation is also studied (**Fig. 8**a). The dark reaction was employed for 20 min without H_2O_2, and then H_2O_2 was injected. During the first 20 min after H_2O_2 injection (20-40 min), the diuron removal rates are fast except for Sep, because both degradation and adsorption happened in these materials but only adsorption occurs in Sep. At 80 min, the diuron removal efficiency has reached to 100 % for 61-SepMag, which is faster than the other composite materials with different Fe_3O_4 content. Sep can absorb at least 20 % of diuron but reach saturation immediately and cannot degraded the herbicide totally. So it is a low efficient and lower adsorbing capacity sorbent individually. For Mag (**Fig. 5 (b)**) and magnetite purchased from the mining company (MagCom) (**Fig. S2**), the agglomeration and crystal size is much larger, reach to 5~60 μm and 10~50 μm, respectively, which leads to less active and reaction sites. However after loaded onto the surface of sepiolite fibers, the crystal size of magnetite sharply decreased to dozens of nanometers and the distribution of magnetite was almost uniform (**Fig. 5**). So the fast reaction rate of 61-SepMag is attributed to the well dispersion and nanocrystallization of magnetite. Sepiolite as catalyst carrier and ordinary sorbent shows positive reinforcement function. Sep also has other advantages such as low-cost, high chemical stability, large specific surface area and large thermal stability and have been used as catalyst support in a lot of areas.

The effect of ultrasound intensity on the diuron degradation is shown (**Fig. 8**b). With increasing ultrasound power from 120 W to 300 W, the degradation rate increases linearly and reaches the peak value at 300 W. And the diuron degradation rate at 300 W seems similar to that at 600 W. For “0 W”, we use stirring method to replace the ultrasonic method. It is seen that the ultrasound methods with ultrasound radiation are much faster than stirring method. This higher removal efficiency may be attributed to the direct relationship between Fenton's reagent and the ultrasonic irradiation. The traditional reaction in stirring systems can be shown with Reactions 3-5 (Wei et al., 2017):

284 $$\bullet OH + diuron \rightarrow \text{degradation products} \quad (3)$$

285 $$Fe^{2+} + H_2O_2 \rightarrow Fe^{3+} + OH^- + \bullet OH \quad (4)$$

286 $$Fe^{3+} + H_2O_2 \rightarrow Fe^{2+} + \bullet OOH + H^+ \quad (5)$$

287 But ultrasound/SepMag/H_2O_2 system improved the conventional Fenton reaction system,
288 showing in three parts as follows (Ayanda et al., 2018a). During sonication, transient collapse
289 of cavitation bubbles generates •OH, •H and •HO_2 radicals (Reactions 6-8). The))) represents
290 the ultrasound:

291 $$H_2O \xrightarrow{)))} \bullet H + \bullet OH \quad (6)$$

292 $$\bullet OH + \bullet OH \rightarrow H_2 + O_2 \quad (7)$$

293 $$\bullet H + O_2 \rightarrow \bullet HO_2 \quad (8)$$

294 Following the H_2O_2 assisted ultrasound, the thermal decomposition of H_2O_2 in the cavitation
295 bubbles forms reactive radicals (Reactions 9-11):

296 $$H_2O_2 \xrightarrow{)))} \bullet OH + \bullet OH \quad (9)$$

297 $$H_2O_2 + O_2 \xrightarrow{)))} 2\bullet HO_2 \quad (10)$$

298 $$H_2O_2 + \bullet OH \rightarrow \bullet HO_2 + H_2O \quad (11)$$

299 And as for SepMag/H_2O_2 assisted ultrasound, the SepMag particles enhanced the generation
300 of cavitation bubbles from the composite particles which act as the nucleation sites (Shchukin
301 et al., 2011; Cravotto et al., 2013). Ultrasound also make for regeneration of Fe^{2+} which could
302 react with H_2O_2 and produce more hydroxyl radical (Reactions 12-14):

303 $$Fe^{2+} + H_2O_2 \rightarrow \bullet OH + OH^- + Fe^{3+} \quad (12)$$

304 $$Fe^{3+} + H_2O_2 \rightarrow Fe\text{-}O_2H^{2+} + H^+ \quad (13)$$

305 $$Fe\text{-}O_2H^{2+} \xrightarrow{)))} Fe^{2+} + \bullet HO_2 \quad (14)$$

306 Another reason for the high efficiency of the ultrasound/SepMag/H_2O_2 system may be
307 due to the fact that the ultrasound irradiation dispersed the aggregated SepMag in aqueous

solution, and thus resulted in more contact areas between Mag and H_2O_2 (Xu et al., 2013). Meanwhile, ultrasound can also decontaminate the composite surface to remove the attached intermediates and impurities to prevent blocking and thus increase the activation of H_2O_2. Hence, ultrasound had an effective role in the effective generation of hydroxyl radical in ultrasound/SepMag/H_2O_2 system due to the synergistic effect from material surface, H_2O_2 and regeneration of Fe^{2+} (Ayanda et al., 2018b; Jaafarzadeh et al., 2018). Diuron is rapidly and efficiently removed by the ultrasound SepMag system, hence, it is also important to investigate diuron degradation mechanism under these conditions. Firstly, mineralization of diuron by ultrasound SepMag system was evaluated using total organic carbon (TOC). Similar to other AOPs, TOC removal in this process was efficient and 65.14% diuron were mineralized to CO_2 after 2 h reaction (Table S1), which is much higher than conventional system without the help of ultrasound (Yi et al., 2016).

HPLC–MS was used to determine the oxidation products of diuron. The results indicated that diuron could be converted to other organic molecules with low molecular weight. After oxidation of diuron, five intermediates have been accurately identified with mass-to-charge ratios (*m/z*) of 219.0, 249.0, 265.0, 215.1 and 165.1 (**Fig. 9**, Fig. S3-S6). Additionally, low-mass products were also observed only in the degraded diuron. These ions were not observed in blanks or in diuron prior to degradation. Based on these results, a proposed degradation pathway of diuron by ultrasound SepMag system was presented in **Fig. 10**. There are two main sites of attack by radicals: the aromatic ring and the methyl groups. The product with *m*/*z*=219.0 belongs to oxidation of the methyl groups. On the other hand, other products were from dehalogenation or hydroxylation reaction. Then these products were subsequently oxidized to other intermediates with smaller molecular weight and these intermediates may be the same with (Yi et al., 2016), but they are not detected in our research. Finally, after the opening of the phenyl ring, all organics would be further transformed to inorganics that

cannot be observed by HPLC-MS, such as CO_2, H_2O, etc. As shown in **Fig. 11**, the binding energy of fresh SepMag located at 710.3 eV, 711.2 eV and 712.7 eV represented the Fe^{2+} in octahedral (Oh) sites, Fe^{3+} in octahedral (Oh) sites, and Fe^{3+} in tetrahedral (Td) sites. For Fe_3O_4, it could be expressed to $FeO{\cdot}Fe_2O_3$, and the Fe^{2+}:Fe^{3+} ratio should be 1:2 via stoichiometry evaluation and the Fe^{2+}:Fe^{3+} ratio in this study was 1:1.9, which is slightly higher. For used SepMag, the peak located at 711.2 eV was shifted to 710.9 eV for Fe^{2+}(Oh), the peak at 710.3 eV was transferred to 710 eV for Fe^{3+}(Oh) and the peak from 712.7 eV to 712.5 eV for Fe^{3+}(Td), which could be attributed to the electron transfer between Fe^{2+} and Fe^{3+} during the degradation reaction, although the ratio of Fe^{2+}:Fe^{3+} became 1:1.7, and did not change obviously (Wilson and Langell, 2014; Lai et al., 2018).

4. Conclusions

The SepMag composites were synthesized by a co-precipitation method. The composite exhibited a notable catalytic activity for diuron degradation, compared to Mag, Sep and Mag from a company. Diuron degradation by SepMag/H_2O_2 system was enhanced under ultrasound treatment. The 61-SepMag composite shows the best degradation efficiency with the optimized degradation condition (1 g/L composite, pH=3, 40 mM H_2O_2, 300 W ultrasonic intensity). The temperature was found to have a positive influence on the degradation rate of diuron. Mineralization of diuron by ultrasound assisted SepMag/H_2O_2 system were investigated and a degradation pathway was proposed, and also the electron transfer was determined between Fe^{2+} and Fe^{3+} in SepMag composites during the degradation reaction for diuron.

Acknowledgements

This work was financially supported by QUT Science and Engineering Faculty and the

Institute for Future Environments, the National Key R&D Program of China (2017YFB0310903), the National Science Fund for distinguished Young Scholars (51225403), the Strategic Priority Research Program of Central South University (ZLXD2017005), the Hunan Provincial Science and Technology Project (2016RS2004, 2015TP1006, 2018WK4023) and the Changsha Science and Technology Project (kc1702029). Kai Hou would like to thank David Marshall, Elizabeth Graham, Shane Russell, Jamie Riches, Llew Rintoul and Chris East (QUT) for their friendly help.

References

Ahribesh, A.A., Lazarević, S., Janković-Častvan, I., Jokić, B., Spasojević, V., Radetić, T., Janaćković, Đ., Petrović, R., 2017. Influence of the synthesis parameters on the properties of the sepiolite-based magnetic adsorbents. Powder Technology 305, 260-269.

Akkari, M., Aranda, P., Ben Rhaiem, H., Ben Haj Amara, A., Ruiz-Hitzky, E., 2016. ZnO/clay nanoarchitectures: Synthesis, characterization and evaluation as photocatalysts. Applied Clay Science 131, 131-139.

Akkari, M., Aranda, P., Mayoral, A., Garcia-Hernandez, M., Ben Haj Amara, A., Ruiz-Hitzky, E., 2017. Sepiolite nanoplatform for the simultaneous assembly of magnetite and zinc oxide nanoparticles as photocatalyst for improving removal of organic pollutants. Journal of Hazardous Materials 340, 281-290.

Akyuz, S., Akyuz, T., Akalin, E., 2010. Adsorption of isoniazid onto sepiolite–palygorskite group of clays: An IR study. Spectrochimica Acta Part A: Molecular and Biomolecular Spectroscopy 75, 1304-1307.

Allan, H.L., van de Merwe, J.P., Finlayson, K.A., O'Brien, J.W., Mueller, J.F., Leusch, F.D.L., 2017. Analysis of sugarcane herbicides in marine turtle nesting areas and assessment of risk using in vitro toxicity assays. Chemosphere 185, 656-664.

Arshad, A., Iqbal, J., Ahmad, I., Israr, M., 2018. Graphene/Fe_3O_4 nanocomposite: Interplay between photo-Fenton type reaction, and carbon purity for the removal of methyl orange. Ceramics International 44, 2643-2648.

Ayanda, O.S., Nelana, S.M., Naidoo, E.B., 2018. Ultrasonic degradation of aqueous phenolsulfonphthalein (PSP) in the presence of nano-Fe/H_2O_2. Ultrasonics Sonochemistry 47, 29-35.

Burgos-Castillo, R., Sillanpaa, M., Brillas, E., Sires, I., 2018. Removal of metals and phosphorus recovery from urban anaerobically digested sludge by electro-Fenton treatment. Science of the Total Environment 644, 173-182.

Chang, J., Ma, J., Ma, Q., Zhang, D., Qiao, N., Hu, M., Ma, 2016. Adsorption of methylene blue onto Fe_3O_4/activated montmorillonite nanocomposite. Applied Clay Science 119, 132-140.

Chen, H., Li, Y., Wang, S., Zhou, Y., 2017. Synthesis of montmorillonite/Fe_3O_4-OTAB composite capable of using as anisotropic nanoparticles. Applied Surface Science 402, 384-391.

Chen, L., Zhou, C.H., Fiore, S., Tong, D.S., Zhang, H., Li, C.S., Ji, S.F., Yu, W.H., 2016. Functional magnetic nanoparticle/clay mineral nanocomposites: preparation, magnetism and versatile applications. Applied Clay Science 127-128, 143-163.

Cravotto, G., Gaudino, E.C., Cintas, P., 2013. On the mechanochemical activation by ultrasound. Chemical Society Reviews 42, 7521-7534.

De Valck, J., Rolfe, J., 2018. Linking water quality impacts and benefits of ecosystem services in the Great Barrier Reef. Marine Pollution Bulletin 130, 55-66.

Dong, Y.Z., Piao, S.H., Choi, H.J., 2018. Fe_3O_4/sepiolite magnetic composite particles and their magneto-responsive characteristics. Colloid and Polymer Science 296, 11-19.

Fayazi, M., Afzali, D., Taher, M.A., Mostafavi, A., Gupta, V.K., 2015. Removal of Safranin dye from aqueous solution using magnetic mesoporous clay: Optimization study. Journal of Molecular Liquids 212, 675-685.

Gonzalez-Alfaro, Y., Aranda, P., Fernandes, F.M., Wicklein, B., Darder, M., Ruiz-Hitzky, E., 2011. Multifunctional porous materials through ferrofluids. Advanced Materials 23, 5224-5228.

Hajba, L., Guttman, A., 2016. The use of magnetic nanoparticles in cancer theranostics: Toward handheld diagnostic devices. Biotechnology Advances 34, 354-361.

Hou, K., Wen, X., Yan, P., Tang, A., Yang, H., 2017. Tin Oxide-Carbon-Coated Sepiolite Nanofibers with Enhanced Lithium-Ion Storage Property. Nanoscale Research Letters 12, 215.

Jaafarzadeh, N., Takdastan, A., Jorfi, S., Ghanbari, F., Ahmadi, M., Barzegar, G., 2018. The performance study on ultrasonic/Fe_3O_4/H_2O_2 for degradation of azo dye and real textile wastewater treatment. Journal of Molecular Liquids 256, 462-470.

Jeon, P.R., Kim, D.-W., Lee, C.-H., 2018. Dissolution and reaction in a CO_2-brine-clay mineral particle system under geological CO_2 sequestration from subcritical to supercritical conditions. Chemical Engineering Journal 347, 1-11.

Rosas, J.M., Vicente, F., Saguillo, E.G., Santos, A., Romero, A., 2014. Remediation of soil polluted with herbicides by Fenton-like reaction:Kinetic model of diuron degradation. Applied Catalysis B: Environmental, 252-260.

Kuo, W.G., 1992. Decolorizing dye wastewater with Fenton's reagent. Water Research, 26, 881-886.

Khongthon, W., Jovanovic, G., Yokochi, A., Sangvanich, P., Pavarajarn, V., 2016. Degradation of diuron via an electrochemical advanced oxidation process in a microscale-based reactor. Chemical Engineering Journal 292, 298-307.

Lai, L., Zhou, H., Lai, B., 2018. Heterogeneous degradation of bisphenol A by peroxymonosulfate activated

426 with vanadium-titanium magnetite: Performance, transformation pathways and mechanism. Chemical
427 Engineering Journal 349, 633-645.
428 Lenders, J.J.M., Zope, H.R., Yamagishi, A., Bomans, P.H.H., Arakaki, A., Kros, A., de With, G.,
429 Sommerdijk, N.A.J.M., 2015. Bioinspired Magnetite Crystallization Directed by Random
430 Copolypeptides. Advanced Functional Materials 25, 711-719.
431 Li, X., Yang, Q., Ouyang, J., Yang, H., Chang, S., 2016. Chitosan modified halloysite nanotubes as
432 emerging porous microspheres for drug carrier. Applied Clay Science 126, 306-312
433 Liu, Y., Kong, Q.-H., Zhao, X.-M., Zhu, P., Zhao, J., Esteban-Cubillo, A., Santarén, J., Wang, D.-Y., 2017.
434 Effect of Fe_3O_4-doped sepiolite on the flammability and thermal degradation properties of epoxy
435 composites. Polymers for Advanced Technologies 28, 971-978.
436 Long, M., Zhang, Y., Huang, P., Chang, S., Hu, Y., Yang, Q., Mao, L., Yang, H., 2018. Emerging Nanoclay
437 Composite for Effective Hemostasis. Advanced Functional Materials 28, 1704452.
438 Ma, L., He, H., Zhu, R., Zhu, J., Mackinnon, I.D.R., Xi, Y., 2016a. Bisphenol A degradation by a new
439 acidic nano zero-valent iron diatomite composite. Catalysis Science & Technology 6, 6066-6075.
440 Ma, L., Rathnayake, S.I., He, H., Zhu, R., Zhu, J., Ayoko, G.A., Li, J., Xi, Y., 2016b. In situ sequentially
441 generation of acid and ferrous ions for environmental remediation. Chemical Engineering Journal 302,
442 223-232.
443 Ma, Y., Wu, X., Zhang, G., 2017. Core-shell Ag@Pt nanoparticles supported on sepiolite nanofibers for the
444 catalytic reduction of nitrophenols in water: Enhanced catalytic performance and DFT study. Applied
445 Catalysis B: Environmental 205, 262-270.
446 Mahamuni, N.N., Adewuyi, Y.G., 2010. Advanced oxidation processes (AOPs) involving ultrasound for
447 waste water treatment: a review with emphasis on cost estimation. Ultrasonics Sonochemistry 17,
448 990-1003.
449 Mao, H., Zhu, K., Liu, X., Yao, C., Kobayashi, M., 2016. Facile synthetic route to Fe_3O_4/silica
450 nanocomposites pillared clay through cationic surfactant-aliphatic acid mixed system and application
451 for magnetically controlled drug release. Microporous and Mesoporous Materials 225, 216-223.
452 Marins, J.A., Mija, A., Pin, J.-M., Giulieri, F., Soares, B.G., Sbirrazzuoli, N., Lançon, P., Bossis, G., 2015.
453 Anisotropic reinforcement of epoxy-based nanocomposites with aligned magnetite–sepiolite hybrid
454 nanofiller. Composites Science and Technology 112, 34-41.
455 Middea, A., Spinelli, L.S., Souza Jr, F.G., Neumann, R., Fernandes, T.L.A.P., Gomes, O.D.F.M., 2017.
456 Preparation and characterization of an organo-palygorskite-Fe_3O_4 nanomaterial for removal of anionic
457 dyes from wastewater. Applied Clay Science 139, 45-53.
458 Mohammed, L., Gomaa, H.G., Ragab, D., Zhu, J., 2017. Magnetic nanoparticles for environmental and
459 biomedical applications: A review. Particuology 30, 1-14.
460 Nasrabadi, H., Amirghofran, Z., Esmaeilbeig, A., Bahrami, M., Jafar Hoseini, S., 2018. Covalent bonding
461 of magnetic Fe_3O_4 nanoparticles to aminopropyl-functionalized magnesium phyllosilicate clay:

462 Synthesis and cytotoxic potential investigation. Applied Organometallic Chemistry 32, e4036.
463 Nor, Y.A., Zhou, L., Meka, A.K., Xu, C., Niu, Y., Zhang, H., Mitter, N., Mahony, D., Yu, C., 2016.
464 Engineering Iron Oxide Hollow Nanospheres to Enhance Antimicrobial Property: Understanding the
465 Cytotoxic Origin in Organic Rich Environment. Advanced Functional Materials 26, 5408-5418.
466 Oturan, M.A., Oturan, N., Edelahi, M.C., Podvorica, F.I., Kacemi, K.E., 2011. Oxidative degradation of
467 herbicide diuron in aqueous medium by Fenton's reaction based advanced oxidation processes.
468 Chemical Engineering Journal 171, 127-135.
469 Peng, K., Fu, L., Li, X., Ouyang, J., Yang, H., 2017. Stearic acid modified montmorillonite as emerging
470 microcapsules for thermal energy storage. Applied Clay Science 138, 100-106
471 Puente-Urbina, A., Montero-Campos, V., 2017. Porous Materials Modified with Fe_3O_4 Nanoparticles for
472 Arsenic Removal in Drinking Water. Water, Air, & Soil Pollution 228.
473 Rawtani, D., Khatri, N., Tyagi, S., Pandey, G., 2018. Nanotechnology-based recent approaches for sensing
474 and remediation of pesticides. Journal of Environmental Management 206, 749-762.
475 Rosas, J.M., Vicente, F., Saguillo, E.G., Santos, A., Romero, A., 2014. Remediation of soil polluted with
476 herbicides by Fenton-like reaction: Kinetic model of diuron degradation. Applied Catalysis B:
477 Environmental 144, 252-260.
478 Rowen, D.J., Templeman, M.A., Kingsford, M.J., 2017. Herbicide effects on the growth and photosynthetic
479 efficiency of Cassiopea maremetens. Chemosphere 182, 143-148.
480 Shahid, M.K., Phearom, S., Choi, Y.G., 2018. Synthesis of magnetite from raw mill scale and its application
481 for arsenate adsorption from contaminated water. Chemosphere 203, 90-95.
482 Shchukin, D.G., Skorb, E., Belova, V., Mohwald, H., 2011. Ultrasonic cavitation at solid surfaces.
483 Advanced Materials 23, 1922-1934.
484 Singh, V., Kaul, S., Singla, P., Kumar, V., Sandhir, R., Chung, J.H., Garg, P., Singhal, N.K., 2018. Xylanase
485 immobilization on magnetite and magnetite core/shell nanocomposites using two different flexible alkyl
486 length organophosphonates: Linker length and shell effect on enzyme catalytic activity. International
487 Journal of Biological Macromolecules 115, 590-599.
488 Solís, R.R., Rivas, F.J., Martínez-Piernas, A., Agüera, A., 2016. Ozonation, photocatalysis and
489 photocatalytic ozonation of diuron. Intermediates identification. Chemical Engineering Journal 292,
490 72-81.
491 Vengatesan, M.R., Singh, S., Stephen, S., Prasanna, K., Lee, C.W., Mittal, V., 2017. Facile synthesis of
492 thermally reduced graphene oxide-sepiolite nanohybrid via intercalation and thermal reduction method.
493 Applied Clay Science 135, 510-515.
494 Vicente, F., Santos, A., Sagüillo, E.G., Martínez-Villacorta, Á.M., Rosas, J.M., Romero, A., 2012. Diuron
495 abatement in contaminated soil using Fenton-like process. Chemical Engineering Journal 183, 357-364.
496 Wang, N., Zheng, T., Zhang, G., Wang, P., 2016. A review on Fenton-like processes for organic wastewater
497 treatment. Journal of Environmental Chemical Engineering 4, 762-787.

498 Warne, M.S.J., King, O., Smith, R.A., 2018. Ecotoxicity thresholds for ametryn, diuron, hexazinone and
499 simazine in fresh and marine waters. Environmental Science and Pollution Research International 25,
500 3151-3169.
501 Wei, X., Wu, H., Sun, F., 2017. Magnetite/Fe-Al-montmorillonite as a Fenton catalyst with efficient
502 degradation of phenol. Journal of Colloid and Interface Science 504, 611-619.
503 Wilson, D., Langell, M.A., 2014. XPS analysis of oleylamine/oleic acid capped Fe_3O_4 nanoparticles as a
504 function of temperature. Applied Surface Science 303, 6-13.
505 Xu, H., Zeiger, B.W., Suslick, K.S., 2013. Sonochemical synthesis of nanomaterials. Chem Soc Rev 42,
506 2555-2567.
507 Yan, Z., Fu, L., Zuo, X., Yang, H., 2018. Green assembly of stable and uniform silver nanoparticles on 2D
508 silica nanosheets for catalytic reduction of 4-nitrophenol. Applied Catalysis B: Environmental 226,
509 23-30
510 Yang, B., Tian, Z., Zhang, L., Guo, Y., Yan, S., 2015. Enhanced heterogeneous Fenton degradation of
511 Methylene Blue by nanoscale zero valent iron (nZVI) assembled on magnetic Fe_3O_4/reduced graphene
512 oxide. Journal of Water Process Engineering 5, 101-111.
513 Yi, Q., Bu, L., Shi, Z., Zhou, S., 2016. Epigallocatechin-3-gallate-coated Fe_3O_4 as a novel heterogeneous
514 catalyst of peroxymonosulfate for diuron degradation: Performance and mechanism. Chemical
515 Engineering Journal 302, 417-425.
516 Yu, S., Zhai, L., Zhong, S., Qiu, Y., Cheng, L., Ren, X., 2016. Synthesis and structural characterization of
517 magnetite/sepiolite composite and its sorptive properties for Co(II) and Cd(II). Journal of the Taiwan
518 Institute of Chemical Engineers 59, 221-228.
519 Yuan, L., 2017. Magnetically Recoverable Fe_3O_4-Modified Bentonite as a Heterogeneous Catalyst of H_2O_2
520 Activation for Efficient Degradation of Methyl Orange. Polish Journal of Environmental Studies 26,
521 2355-2361.
522 Yuan, P., Liu, D., Fan, M., Yang, D., Zhu, R., Ge, F., Zhu, J., He, H., 2010. Removal of hexavalent
523 chromium [Cr(VI)] from aqueous solutions by the diatomite-supported/unsupported magnetite
524 nanoparticles. Journal of Hazardous Materials 173, 614-621.
525 Zhang, J., Yan, Z., Ouyang, J., Yang, H., Chen, D., 2018. Highly dispersed sepiolite-based organic modified
526 nanofibers for enhanced adsorption of Congo red. Applied Clay Science 157, 76-85.
527 Zhang, Y., Tang, A., Yang, H., Ouyang, J., 2016. Applications and interfaces of halloysite nanocomposites.
528 Applied Clay Science 119, 8-17
529 Zhao, Q., Fu, L., Jiang, D., Ouyang, J., Hu, Y., Yang, H., Xi, Y., 2019. Nanoclay modulated oxygen
530 vacancies of metal oxide. Communications Chemistry 2, 11
531 Zhou, L., Zheng, W., Ji, Y., Zhang, J., Zeng, C., Zhang, Y., Wang, Q., Yang, X., 2013. Ferrous-activated
532 persulfate oxidation of arsenic(III) and diuron in aquatic system. Journal of Hazardous Materials 263 Pt
533 2, 422-430.

534 Zhou, Z., Ouyang, J., Yang, H., Tang, A., 2016. Three-way catalytic performances of Pd loaded
535 halloysite-$Ce_{0.5}Zr_{0.5}O_2$ hybrid materials. Applied Clay Science 121-122, 63-70.

Figures captions

Fig. 1 Synthesis schematic of SepMag composite and Fenton reaction mechanism with ultrasound assist

Fig. 2 XRD patterns of Sep, SepH and SepMag.

Fig. 3 FTIR spectra of SepH, Mag and SepMag.

Fig. 4 N_2 adsorption/desorption isotherms of SepH, Mag and SepMag.

Fig. 5 SEM images of (a) SepH, (b) Mag and (c) SepMag

Fig. 6 TEM mapping images of (a) SepMag, (b) O, (c) Si, (d) Mg and (e) Fe.

Fig. 7 Effects of (a) pH, (b) SepMag content, (c) initial hydrogen peroxide concentration and (d) temperature on diuron removal rate.

Fig. 8 Effects of (a) Fe content and (b) ultrasonic intensity on diuron removal

Fig. 9. Extracted ion chromatograms for reaction of diuron with 61-SepMag/sonication: (a) *m/z* 165.1, (b) *m/z* 219.0, (c) *m/z* 249.0, (d) *m/z* 265.0, and (e) *m/z* 215.1.

Fig. 10 Proposed degradation pathway of diuron by ultrasound SepMag system

Fig. 11 XPS spectra of Fe 2p in SepMag before and after use

552

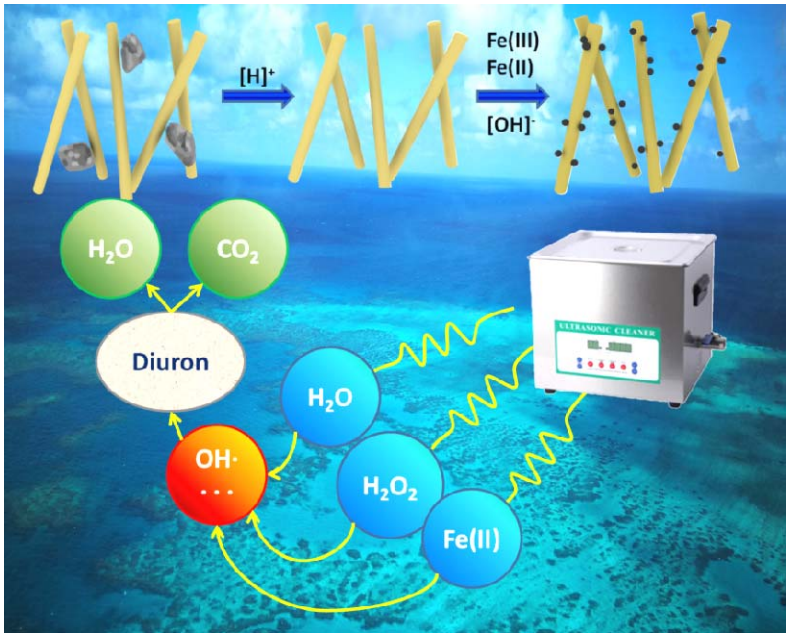

553

554 **Fig. 1** Synthesis schematic of SepMag composite and Fenton reaction mechanism with

555 ultrasound assist

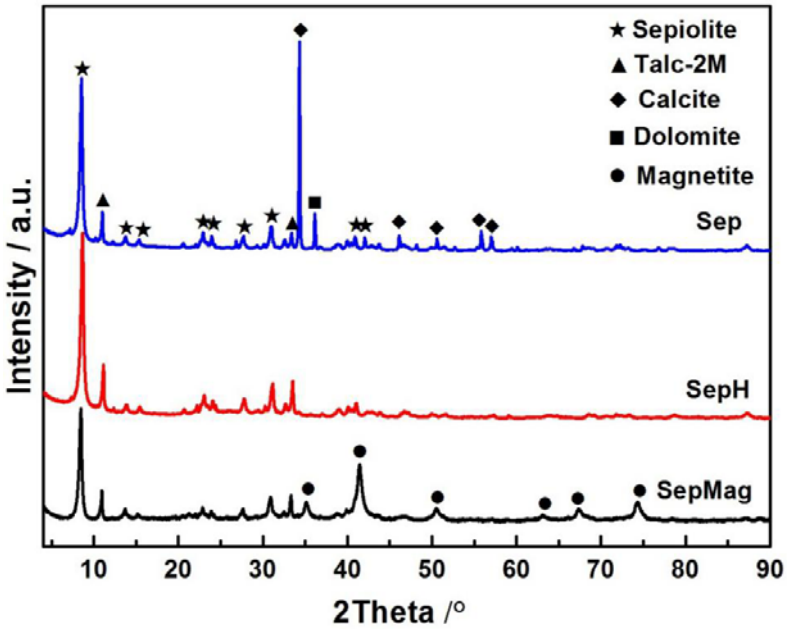

Fig. 2. XRD patterns of Sep, SepH and SepMag.

559

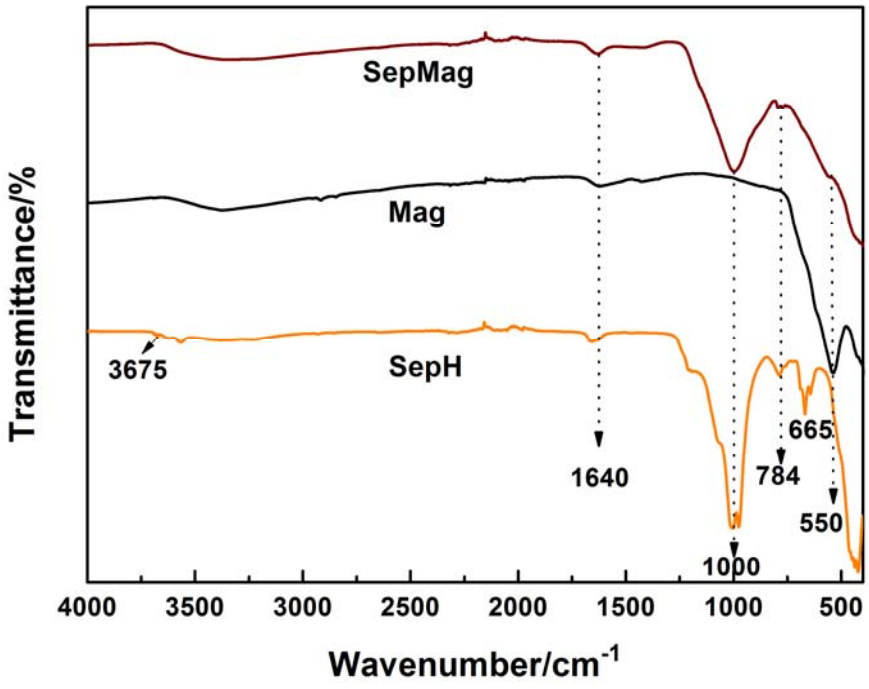

560

561 **Fig. 3.** FTIR spectra of SepH, Mag and SepMag.

562

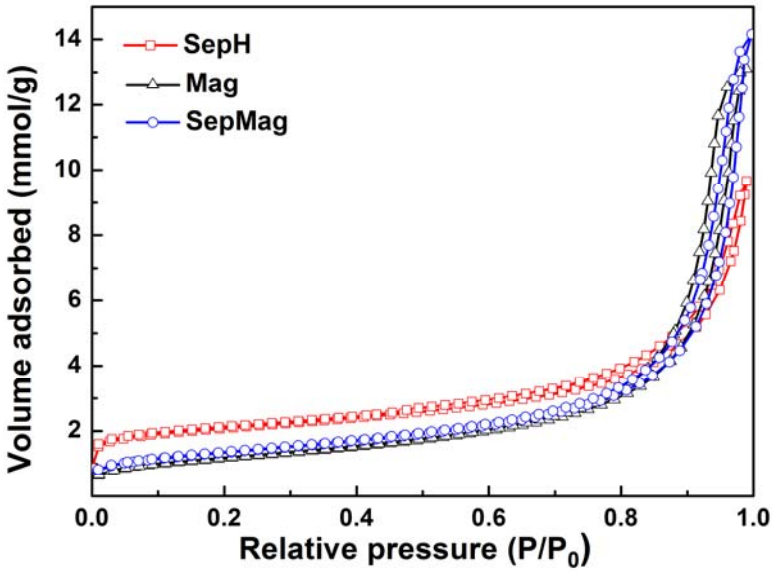

563

564 **Fig. 4.** N_2 adsorption/desorption isotherms of SepH, Mag and SepMag.

565

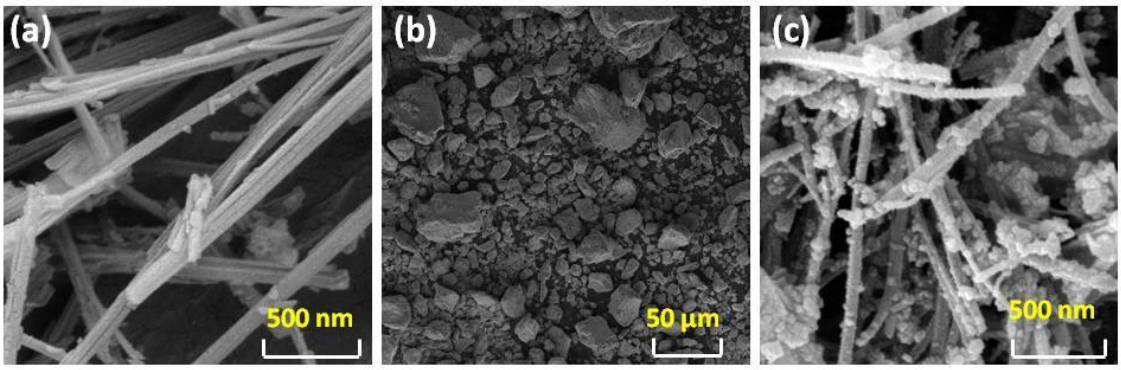

566

567 **Fig. 5.** SEM images of (a) SepH, (b) Mag and (c) SepMag

568

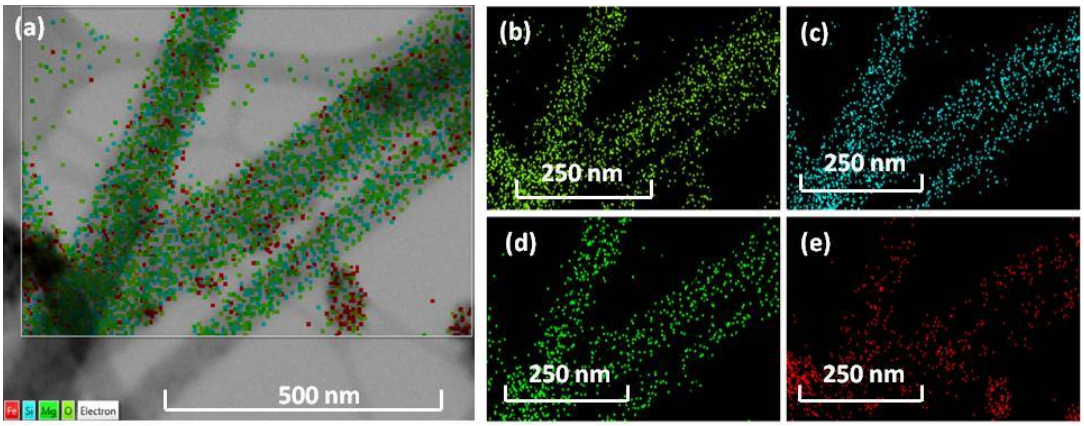

569

570 **Fig. 6.** TEM mapping images of (a) SepMag, (b) O, (c) Si, (d) Mg and (e) Fe.

571

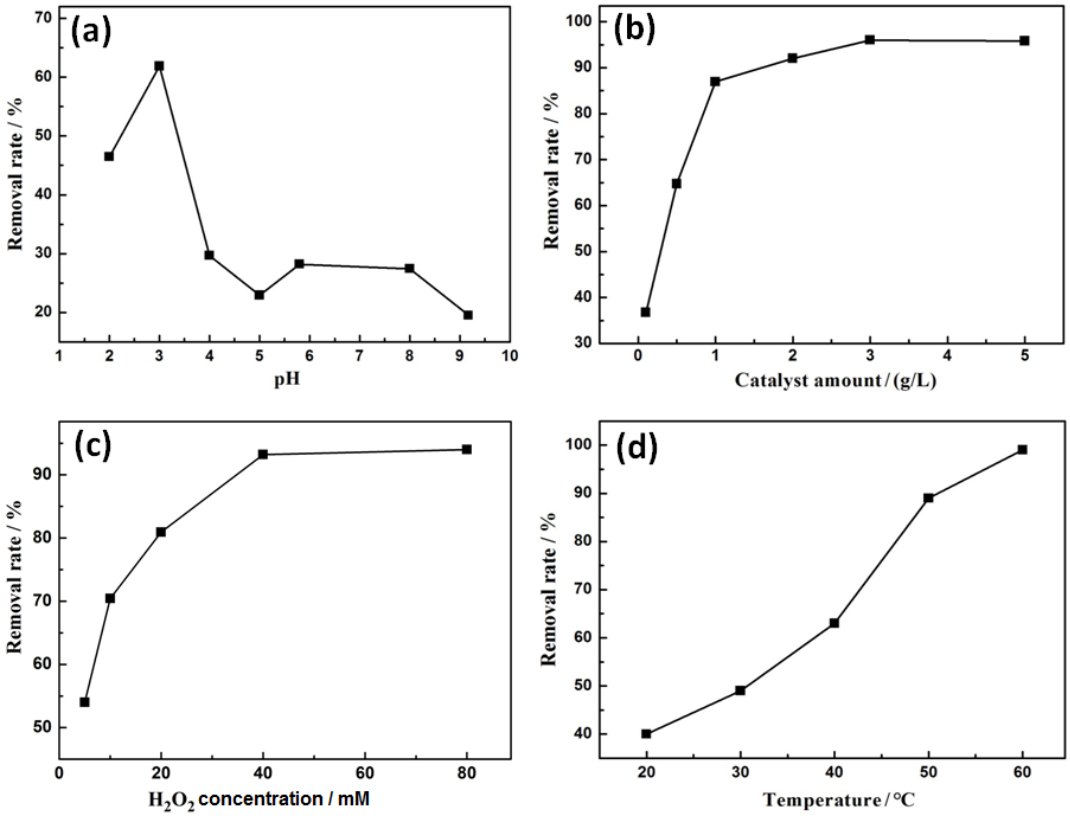

572

573 **Fig. 7.** Effects of (a) pH, (b) SepMag content, (c) initial hydrogen peroxide concentration and

574 (d) temperature on diuron removal rate.

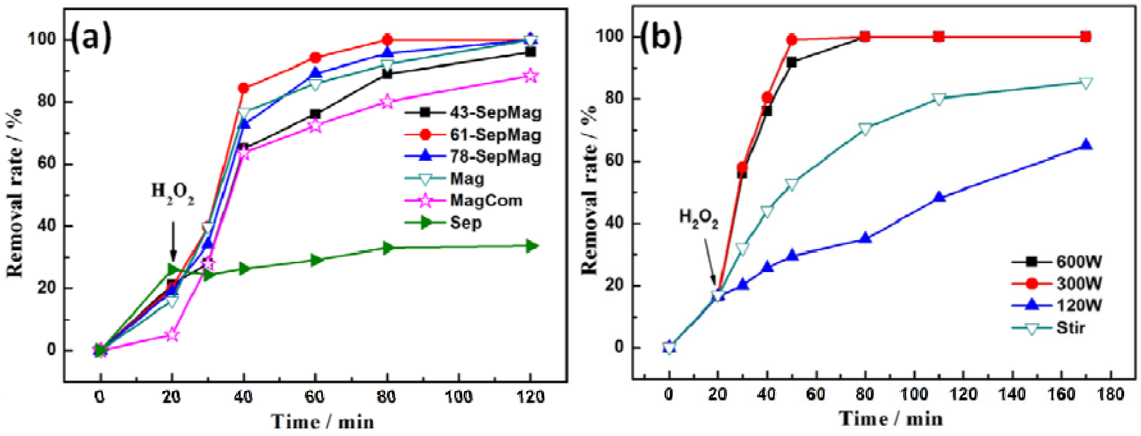

Fig. 8. Effects of (a) Fe content on the degradation of diuron (20 °C, pH 3, 40 mM H_2O_2, 1 g/L sample, 300 W ultrasound power) and (b) ultrasonic intensity on diuron removal (20 °C, pH 3, 40 mM H_2O_2, 1 g/L 61-SepMag).

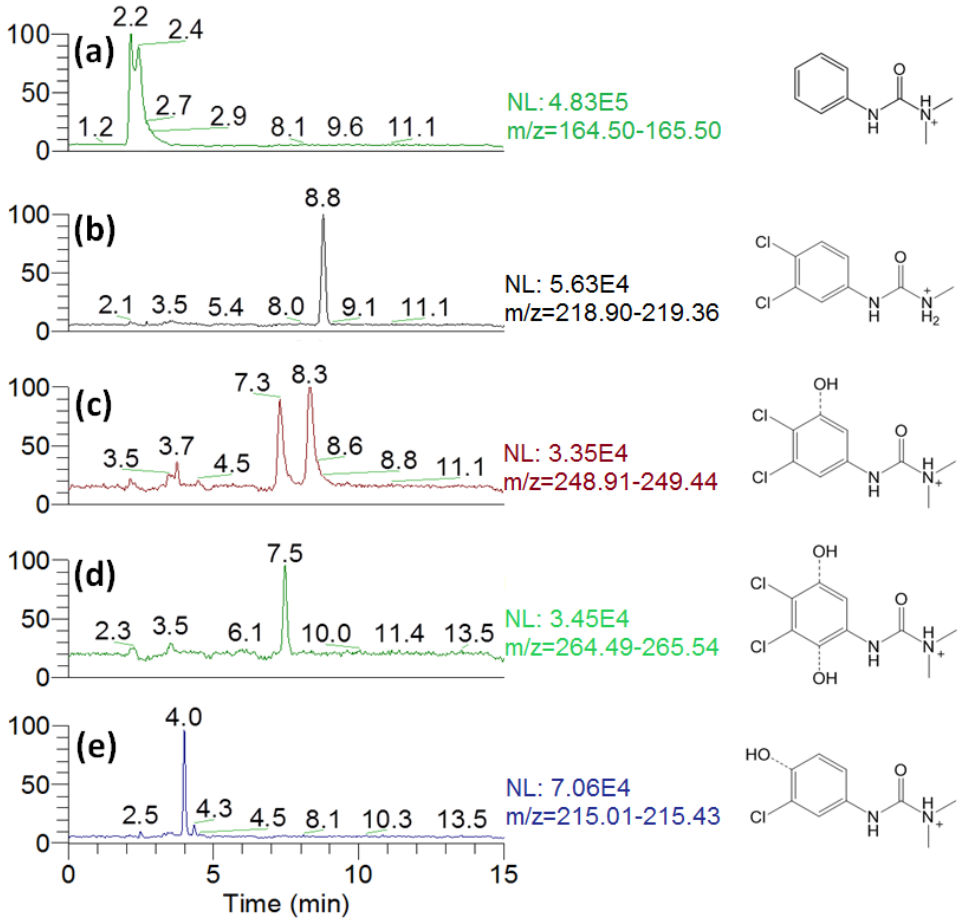

Fig. 9. Extracted ion chromatograms for reaction of diuron with 61-SepMag/sonication: (a) *m/z* 165.1, (b) *m/z* 219.0, (c) *m/z* 249.0, (d) *m/z* 265.0, and (e) *m/z* 215.1. A dashed line (right, structural formula) indicates that the position of OH substitution on the ring is uncertain. The presence of chlorine atom(s) is confirmed by the distinctive isotope abundance pattern ($^{37}Cl/^{35}Cl$) in the mass spectrum.

587

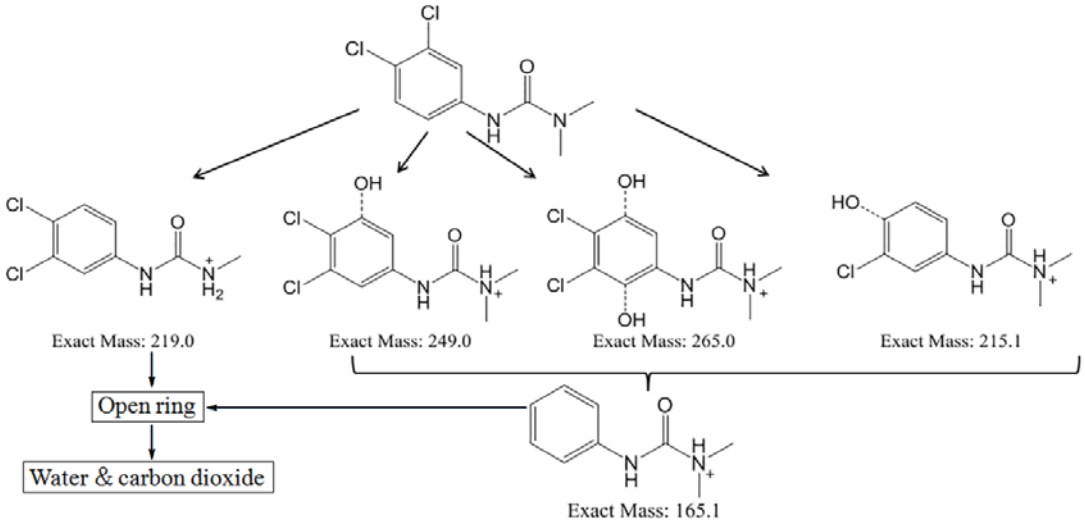

588

589 **Fig. 10.** Proposed degradation pathway of diuron by ultrasound SepMag system

590

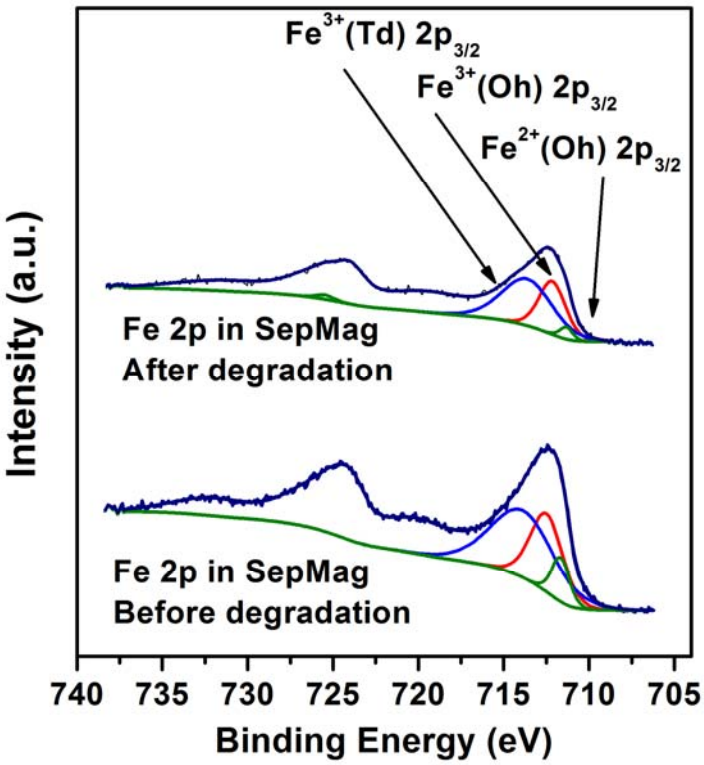

591

592 **Fig. 11.** XPS spectra of Fe 2p in SepMag before and after use.